

Synchronizing Deoxygenation and Hydrogenation to Effect Glycerol Hydrogenolysis over Pt/Nb₂W₁₅O₅₀ at Low H₂ Pressure

ACS Sustainable Chemistry and Engineering

Chen, Jinghu; Huang, Hong; Pan, Hu; Cao, Yongyong; Jiang, Lingchang et al

<https://doi.org/10.1021/acssuschemeng.3c08096>

This publication is made publicly available in the institutional repository of Wageningen University and Research, under the terms of article 25fa of the Dutch Copyright Act, also known as the Amendment Taverne.

Article 25fa states that the author of a short scientific work funded either wholly or partially by Dutch public funds is entitled to make that work publicly available for no consideration following a reasonable period of time after the work was first published, provided that clear reference is made to the source of the first publication of the work.

This publication is distributed using the principles as determined in the Association of Universities in the Netherlands (VSNU) 'Article 25fa implementation' project. According to these principles research outputs of researchers employed by Dutch Universities that comply with the legal requirements of Article 25fa of the Dutch Copyright Act are distributed online and free of cost or other barriers in institutional repositories. Research outputs are distributed six months after their first online publication in the original published version and with proper attribution to the source of the original publication.

You are permitted to download and use the publication for personal purposes. All rights remain with the author(s) and / or copyright owner(s) of this work. Any use of the publication or parts of it other than authorised under article 25fa of the Dutch Copyright act is prohibited. Wageningen University & Research and the author(s) of this publication shall not be held responsible or liable for any damages resulting from your (re)use of this publication.

For questions regarding the public availability of this publication please contact openaccess.library@wur.nl

Synchronizing Deoxygenation and Hydrogenation to Effect Glycerol Hydrogenolysis over Pt/Nb₂W₁₅O₅₀ at Low H₂ Pressure

Jinghu Chen, Hong Huang, Hu Pan, Yongyong Cao, Lingchang Jiang, Qineng Xia,* Xiangtong Meng, Jieshan Qiu, Han Zuilhof, and Shaomin Liu*

Cite This: *ACS Sustainable Chem. Eng.* 2024, 12, 6242–6251

Read Online

ACCESS |

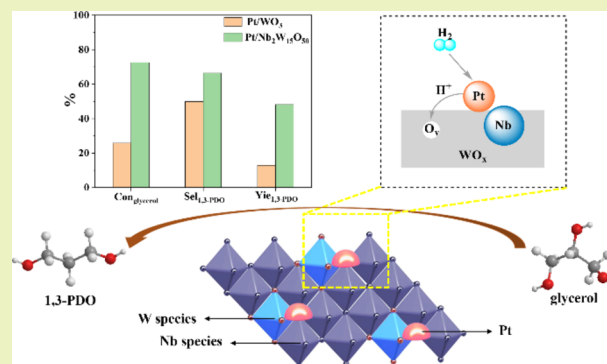
Metrics & More

Article Recommendations

Supporting Information

ABSTRACT: The selective hydrogenolysis of glycerol to 1,3-propanediol (1,3-PDO) necessitates the precise tandem reactions of deoxygenation at a specific location and the ensuing hydrogenation steps. Herein, a solid solution-supported catalyst Pt/Nb₂W₁₅O₅₀ was reported for the hydrogenolysis of glycerol to 1,3-PDO. We engineered the exceptional interaction between active Pt and oxygen vacancies to efficiently integrate the deoxygenation and hydrogenation steps in tandem. The strong interaction between active Pt and oxygen vacancies was established via hydrogen (H₂) spillover and induced the generation of 1,3-PDO in situ. This synergistic effect confers Pt/Nb₂W₁₅O₅₀ with high catalytic performance, combining a 75.6% conversion of glycerol and 66.5% selectivity to 1,3-PDO at a low H₂ pressure of 1.0 MPa (noting that most catalysts require H₂ pressures of ≥4 MPa). Moreover, the structure–performance relationship validated that there is a linear correlation between active Pt, oxygen vacancies, and 1,3-PDO yield. This study provides mechanistic insights into further catalyst developments for the valorization of other biomass-derived oxygenates.

KEYWORDS: Pt/Nb₂W₁₅O₅₀ active Pt, oxygen vacancies, H₂ spillover, low H₂ pressure



INTRODUCTION

To pursue the vision of sustainable development, the green and low-carbon transformation of global energy will become an important way to coordinate the common development of energy, environment, and economy.^{1,2} Valorization of over-capacity glycerol (the main byproduct of biodiesel) can not only reduce energy waste and environmental problems but also obtain economic benefits and expand the biodiesel industry chain. In this context, the catalytic conversion of glycerol into value-added chemicals is considered to be one of the most promising chemical upgrading reactions.^{3–5} When assessing the downstream derivatives, specifically, 1,3-PDO seems to have a high potential given by its large use in the polyester fiber field and its already wide application in textile, food, cosmetics, pharmaceutical, and other industries.⁶ Yet, it is difficult to achieve the precise activation and cleavage of this secondary C–O band in glycerol hydrogenolysis, as it is limited by steric hindrance and thermodynamic factors.⁷ However, glycerol valorization to 1,3-PDO is advanced specifically by hydrogenolysis reactions catalyzed over heterogeneous catalysts, which requires optimization of the near-synchronous deoxygenation and hydrogenation steps.⁸ In the 1980s, Che et al. pioneered the formation of 1,3-PDO in glycerol hydrogenolysis, to provide a 21% yield.⁹ In recent years, the steady progression of catalyst design has allowed the yield to increase

to 76%.¹⁰ Based on such research, the most promising candidate for an optimal catalyst appears to be the loading of noble metals on an oxyphilic metal oxide, as these correspond to hydrogenation- and deoxygenation-active centers, respectively. The catalytic performance of different catalysts for glycerol hydrogenolysis to 1,3-PDO is listed in Table S1. Especially, Pt–W- and Ir–Re-based catalysts have in this regard evolved as prototypical examples.⁷ Although Ir–Re-based catalysts have high selectivity, they were limited by low yield and high cost. Considering the feasibility of production, Pt–W-based catalysts have become the main candidates due to their stable yield and relatively lower cost.

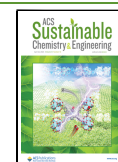
In these initial studies, the pursuit of a maximized 1,3-PDO yield was the prime goal, in view of its economic potential, but as a concomitant result, the intrinsic relationship between the precise catalyst structure, the detailed mechanism, and the improved performance did not attract equal attention. More recently, the mechanism has started to receive more detailed

Received: December 9, 2023

Revised: March 22, 2024

Accepted: March 27, 2024

Published: April 10, 2024



attention, and following the concept of a bifunctional catalyst, strategies such as doping, acid site modulation, and structure regulation have led to a focus on establishing structure–performance relationships.^{11–13} This yielded that specific active centers, such as Brønsted acid sites, can positively affect the selectivity of the reduction of secondary C–O bonds.^{14,15} Recently, Fu's team modulated the dynamics of Brønsted acid sites on a Pt/WO_x catalyst to drive the selective activation of the secondary C–O bond and reached an order of magnitude increase in the dehydration average reaction rate under the action of periodic hydrogen pulses.¹⁶ With an eye to analogous control over the Brønsted acid site, Fan et al. selected different phases of ZrO₂-supported Pt–W catalysts, which display a diversity of acid sites.¹⁷ Pt-WO_x/t-ZrO₂ catalysts with more Brønsted acid sites were favorable for the formation of 1,3-PDO. Even so, subtle changes in the catalyst structure upon the regenerative reduction of the surface (formation of Pt(0) and W(V)) make it difficult to directly link the precise catalyst structure to the observed performance, thus hampering detailed mechanistic insights. The generation of dynamic active sites was intimately coupled with catalyst reducibility. The coupling of these different but near-synchronous processes makes it difficult to directly link the catalytic mechanism to the overall catalytic performance.¹⁶ On the other hand, researchers believe that H₂ spillover exists in the redox reaction involving H₂.¹⁸ The electron migration induced by this spillover strengthens the interaction between the support and the noble metal.¹⁹ Choi et al. encapsulated platinum in an aluminosilicate matrix with controlled diffusion properties, elucidating that surface hydroxyls (presumably Brønsted acids) are essential for the utilization of H₂ spillover on the support surface.²⁰ Afterward, a linear relationship between the amount of Pt-bound H (H/Pt) and the overall glycerol conversion was discovered by carefully adjusting the H₂ spillover capacity of the catalyst.²¹ This indicated that H₂ spillover is of great significance in the glycerol hydrogenolysis on WO₃-rich nanocatalysts.

Obviously, the acid sites and H₂ spillover mentioned above are related to the deoxygenation- and hydrogenation-active centers of the bifunctional system, respectively. Therefore, to successfully drive the deoxygenation–hydrogenation tandem reaction, it is necessary to effectively integrate the two active centers. However, this makes the exploration of interactions even more difficult, as changes in the electronic structure and unsaturated coordination environment resulting from the interactions between these active centers are prone to generate defects in the catalysts, especially in metal oxides.²² The effects of defects on the catalytic performance are easily overlooked, as they are often difficult to identify and an almost intrinsic feature of the coupling of the deoxygenation and hydrogenation reactions.

In this article, we developed a sol-assisted cationic coordination assembly strategy to synthesize a solid solution-supported catalyst Pt/Nb₂W₁₅O₅₀. Multiple structural characterization and *in situ* DRIFTS measurements were used to clarify the formation and connection between active Pt and oxygen vacancies. In this study, we aimed to further elucidate the mechanism and to find reaction conditions in which a high selectivity can be combined with a low H₂ pressure, as the latter would effectively reduce the costs associated with industrial operation. Combined with activity test results, structure–performance relationships were established, which

further elucidate the mechanistic links between active Pt and oxygen vacancies.

EXPERIMENTAL SECTION

Chemicals and Materials. Ammonium hydroxide (NH₃·H₂O), hydrogen peroxide (H₂O₂), ethylene glycol ((CH₂OH)₂), glycerol, 1,2-PDO, 1,3-PDO, *i*-PO, *n*-PO, and 1,4-butanediol (1,4-BDO) were obtained from Sinopharm Chemical Reagent Co. Ltd. Citric acid (C₆H₈O₇), ammonium metatungstate ((NH₄)₆(H₂W₁₂O₄₀)·*n*H₂O), and platinum(II)nitrate (Pt(NO₃)₂) were purchased from Aladdin Reagent, and niobium oxide (Nb₂O₅) was produced from Sinopharm Chemical Reagent Co. Ltd. All of the above were directly used without further purification. Hydrogen–Argon (H₂–Ar) (10% H₂), high-purity grade hydrogen (H₂, ≥99.9%), air, and nitrogen (N₂, ≥99.9%) were purchased from Beijing Shunan Fancy Gas Co., Ltd.

Catalyst Preparation. 15 g of citric acid, 15 mmol of (NH₄)₆(H₂W₁₂O₄₀)·*n*H₂O, and 2 mmol of niobium hydroxide (Nb(OH)₅) were dissolved in 100 mL of deionized water; the preparation of Nb(OH)₅ has been reported before.¹⁰ 5 mL of (CH₂OH)₂ (AR, 99%) was introduced into the mixture to promote the dispersion of components. Then, 5 mL of H₂O₂ (AR, 30 wt % in H₂O) was added. After being mixed thoroughly, NH₃·H₂O was used to bring the pH value to 3.5. The solution was slowly heated to dry at 90 °C for 5 days to form a sol and calcined at 800 °C for 5 h to obtain Nb–W support. Using the same sol–gel method, (NH₄)₆(H₂W₁₂O₄₀)·*n*H₂O was added only to obtain WO₃.

Pt(NO₃)₂ as the precursor of Pt was loaded onto Nb–W support by incipient wetness impregnation, the loading of Pt was 3 wt %. The impregnated sample was dried at 110 °C for 12 h and then calcined at 350 °C for 4 h to obtain Pt/Nb₂W₁₅O₅₀. Using the same impregnation method, Pt was loaded onto the WO₃ support to obtain the comparative sample Pt/WO₃.

Characterization of Catalysts. Scanning electron microscopy (SEM) images were obtained with a ZEISS GeminiSEM 300 scanning electron microscope (acceleration voltage = 3 kV).

High-resolution transmission electron microscopy (HRTEM) images were obtained on a JEM-2100F microscope operated at 200 kV and equipped with an energy-dispersive X-ray spectroscopy (EDS) microanalysis system. The particle size distributions of Pt nanoparticles were obtained using a Nano measurer.

The nitrogen adsorption and desorption isotherms were collected at 77 K and obtained by the application of the Brunauer–Emmett–Teller (BET) analysis method. The pore size distributions (PSD) were calculated using a Barrett–Joyner–Halenda (BJH) model.

X-ray diffraction (XRD) patterns were recorded on a Rigaku Ultimate IV instrument in the scanning range 5–80° at a speed of 2° min^{−1} with a Cu Kα radiation source operated at a tube voltage of 40 kV and a current of 40 mA.

High-angle annular dark-field scanning transmission electron microscopy (HAADF-STEM) images were acquired on a JEM-2100F electron microscope operated at 200 kV; for these images, the catalyst was evenly dispersed into ethanol and carefully dropped onto a copper grid to be measured.

Temperature-programmed reduction of hydrogen (H₂-TPR) was performed on a Micromeritics Auto Chem II 2920 chemical adsorption analyzer; for such measurements, a 100 mg of the sample was weighed and placed in a U-shaped quartz tube, dried, and pretreated in He at 300 °C for 1 h. After cooling to room temperature and introducing a 10% H₂/Ar mixture flowing gas (50 mL min^{−1}) for 0.5 h, which allowed the baseline to stabilize, the sample was heated to 1200 °C at a ramp of 10 °C min^{−1}. The amount of H₂ consumption was detected and calculated by a thermal conductivity detector (TCD).

Thermal gravimetric analysis (TGA) was conducted on a NETZCH STA-449C thermal analyzer system in the air of catalysts, measuring temperature from room temperature to 800 °C.

X-ray photoelectron spectra (XPS) were performed on a Thermo ESCALAB 250XI spectrometer equipped with an Al Kα radiation source (working voltage = 12.5 kV; filament current = 16 mA; pass

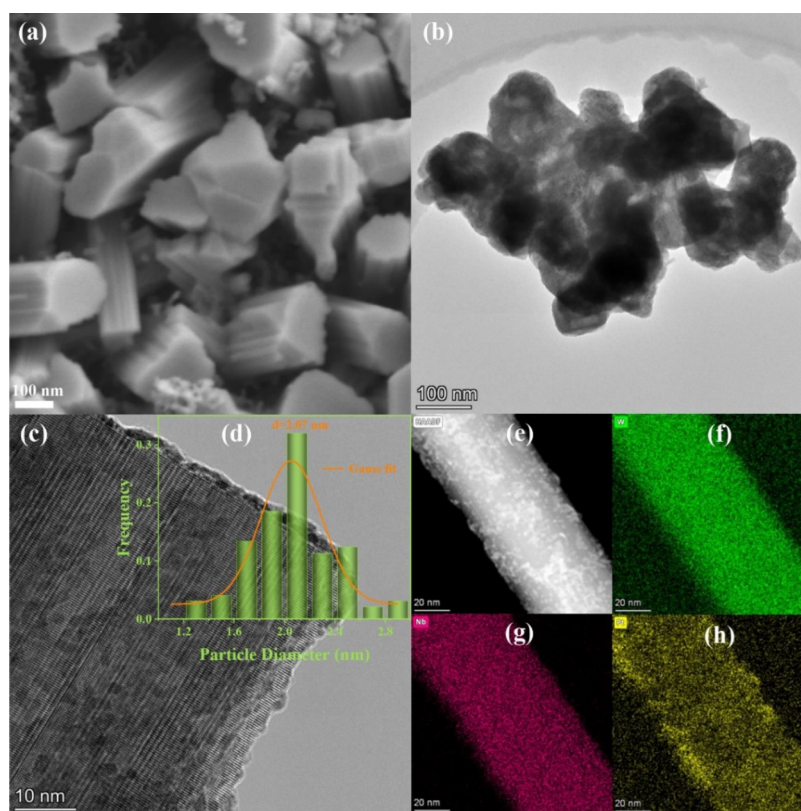


Figure 1. Electron microscope images of Pt/Nb₂W₁₅O₅₀. (a) SEM images, (b, c) HRTEM images, and (d) particle size distributions of Pt nanoparticles. (e) EDS mapping images of Pt/Nb₂W₁₅O₅₀. (f) W, (g) Nb, and (h) Pt.

energy for full spectrum scanning = 100 eV). All binding energies were calibrated with reference to the C 1s peak at 284.8 eV, and the narrow spectrum of Pt and W elements was deconvolution fitted. The catalyst was tested after the reduction treatment. The detailed steps of pretreatment are as follows: the sample was reduced in a H₂ atmosphere at 350 °C for 1 h. Subsequently, the samples were passivated in a N₂ atmosphere for 1 h, and then cooled to room temperature to be measured.

Raman spectra were obtained on a Scientific LabRAM HR Evolution spectrometer in the range 0–1500 cm⁻¹ under a 532 nm excitation laser. The catalyst was tested after reduction treatment, and the pretreatment method is consistent with that of the XPS test.

X-band electron paramagnetic resonance (EPR) was performed on a Bruker E500 EPR spectrometer at room temperature. The catalyst was tested after reduction treatment, and the pretreatment method is consistent with that of the XPS test.

Temperature-programmed desorption of NH₃ (NH₃-TPD) was carried out on the same instrument of H₂-TPR. About 100 mg of the sample was pretreated in a He atmosphere at 300 °C for 1 h; after subsequent cooling to 30 °C, 10% NH₃/He mixture flowing gas (30–50 mL min⁻¹) was introduced for 1 h until adsorption saturation. The tube was purged with a pure He flow for 1 h to remove the weak physical adsorption of NH₃ on the surface. The sample was desorbed and heated to 800 °C at a rate of 10 °C min⁻¹ in a He atmosphere with a record of TCD.

In situ diffuse reflectance infrared Fourier transform spectra of H₂ (DRIFTS-H₂) adsorption were recorded with a Nicolet iS50 Fourier transform infrared (FTIR) spectrometer with an MCT/A detector. About 100 mg of the catalyst was loaded in the high-temperature chamber, and the catalyst was pretreated at 350 °C in a He stream for 0.5 h to remove impurities and moisture. After being cooled to 130 °C (reaction temperature), the background spectrum was recorded. Then, H₂ was introduced for adsorption until adsorption saturation with a continuous record, followed by purging with a He stream to remove physical adsorption of H₂.

In situ DRIFTS of CO adsorption were collected on the same instrument as that used for H₂ adsorption. The method of *in situ* pretreatment of the catalyst is consistent with H₂ adsorption. After pretreatment, the sample was cooled to 130 °C and treated with 10% H₂-Ar flow for 0.5 h, after which the gas flow was switched to a He stream again for 0.5 h to remove any additional physical adsorption of H₂. Cooled to 30 °C, the background was recorded when the spectrum was stable, and then CO was introduced for adsorption, and the adsorption state was recorded continuously, which was followed by purging with He when the CO adsorption reaches saturation.

CO chemisorption was performed on the same instrument as H₂-TPR. About 100 mg of the samples were pretreated in a He atmosphere at 10 °C min⁻¹ from room temperature to 350 °C for 1 h. Subsequently, a 10% H₂-Ar mixture was introduced, and the sample was reduced for 1 h. Cooling to 50 °C, He flow was introduced again to purge the surface H₂ until the baseline was stabilized. The CO pulse titration was performed until the intensity of the elution peak was stable.

In situ DRIFTS of glycerol hydrogenolysis were recorded on the same instrument as used for H₂ and CO adsorption. The pretreatment and prerduction of the samples were consistent with the DRIFTS-CO adsorption experiments. The background spectrum was collected in a He atmosphere at 130 °C. Then glycerol solution was quickly introduced, and a continuous recording spectrum of the reactant adsorption state was started. Next, the atmosphere above the sample was switched to H₂-Ar, the spectra were collected to obtain the reaction state information on glycerol and the products, and finally switched back via He purging until the signal was stable.

Catalytic Reaction. The reaction of glycerol hydrogenolysis was conducted in a 30 mL capacity Teflon-lined stainless-steel autoclave. Reaction conditions: 3 g of 20 wt % glycerol aqueous solution, 0.2 g of catalyst, 1 MPa H₂, 130 °C, 12 h. After the reaction, the liquid phase product was separated by differential centrifugation and analyzed by a gas chromatograph (SP-3530) equipped with a flame ionization detector (FID) and KB-Wax (30 m × 0.25 mm × 0.25 μm) column.

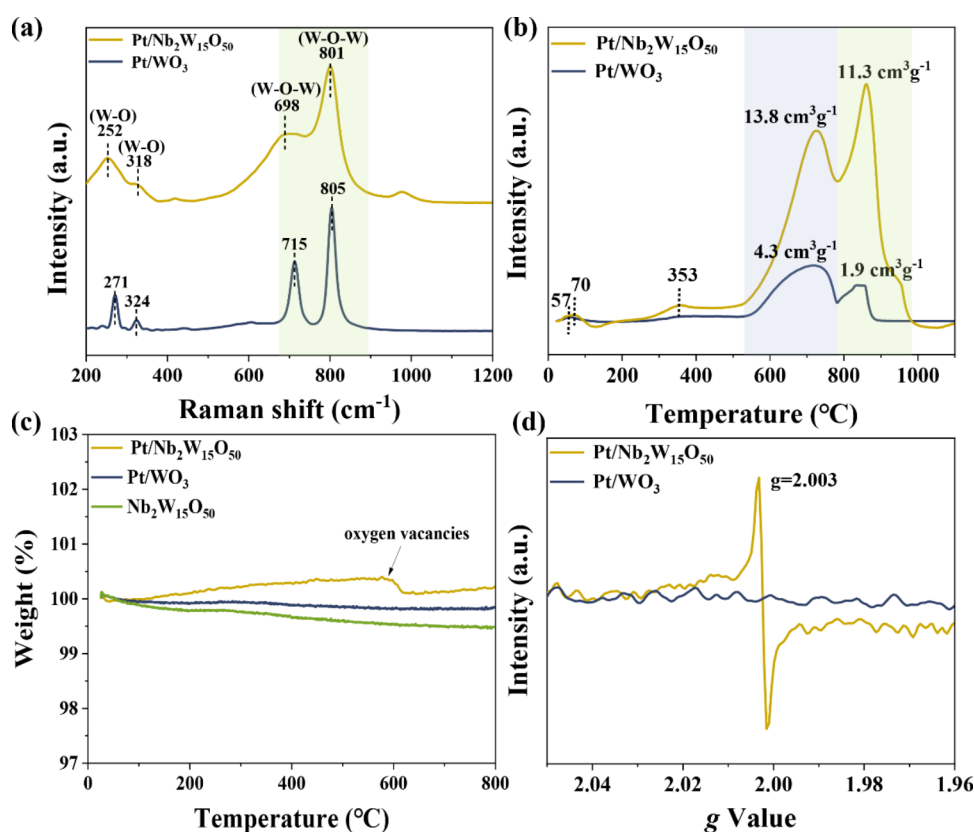


Figure 2. (a) Raman spectra, (b) H_2 -TPR profiles, (c) TGA curves, and (d) EPR spectra of $\text{Pt}/\text{Nb}_2\text{W}_{15}\text{O}_{50}$ and Pt/WO_3 .

Using 1,4-BDO as the internal standard, the liquid products were quantitatively analyzed by the internal standard method. The carbon mass balance was above 95% in all cases, and the selective sum of liquid products was normalized. The conversion of glycerol and the selectivity of each product were calculated using the following equations:

$$\text{Conversion}_{\text{glycerol}} (\%) = (\text{moles}_{\text{glycerol consumed}}) / (\text{moles}_{\text{glycerol fed}})$$

$$\begin{aligned} \text{Selectivity}_{\text{specific product}} (\%) \\ = (\text{moles}_{\text{product observed}} \times \text{stoichiometric factor}) \\ / (\text{moles}_{\text{glycerol consumed}}) \end{aligned}$$

$$\begin{aligned} \text{Yield}_{\text{specific product}} (\%) \\ = \text{Conversion}_{\text{glycerol}} (\%) \times \text{Selectivity}_{\text{specific product}} (\%) \end{aligned}$$

RESULTS AND DISCUSSION

Catalyst Structure. The SEM and HRTEM images of Pt/WO_3 exhibited a jumbled stack of heterogeneous polyhedrons (Figure S1). EDS mapping results demonstrate the uniform dispersion of W and Pt species inside Pt/WO_3 (Figure S1). $\text{Pt}/\text{Nb}_2\text{W}_{15}\text{O}_{50}$ possessed an irregular columnar structure with a diameter of 100–250 nm (Figure 1). Pt nanoparticles with average sizes of 2.15 and 2.07 nm were uniformly dispersed on WO_3 and $\text{Nb}_2\text{W}_{15}\text{O}_{50}$, respectively. The EDS mapping further verified the homogeneous distribution of W, Nb, and Pt inside $\text{Pt}/\text{Nb}_2\text{W}_{15}\text{O}_{50}$. The nitrogen adsorption and desorption isotherms and PSD profiles of the two catalysts and their support are presented in Figure S2. WO_3 and Pt/WO_3 feature a type III adsorption isotherm, implying that both have low

S_{BET} (Table S2). However, $\text{Nb}_2\text{W}_{15}\text{O}_{50}$ and $\text{Pt}/\text{Nb}_2\text{W}_{15}\text{O}_{50}$ feature type-IV isotherms with H1 hysteresis loops, which were assigned as a mesoporous structure. After the incorporation of Pt nanoparticles, the S_{BET} of $\text{Nb}_2\text{W}_{15}\text{O}_{50}$ was decreased from 23 to 10 $\text{m}^2 \text{g}^{-1}$ ($\text{Pt}/\text{Nb}_2\text{W}_{15}\text{O}_{50}$, Table S2), indicating that Pt was anchored to the support surface. Simultaneously, the PSD results revealed a more uniform porosity after the introduction of Pt.

XRD patterns are shown in Figure S3. The Bragg peaks observed at 23.1, 23.6, and 24.4° of Pt/WO_3 were attributed to the (002), (020), and (200) planes of monoclinic phase WO_3 (PDF#83-0950). The addition of Nb changed the WO_3 phase from monoclinic to tetragonal. There are two main crystal planes, (001) and (110), on $\text{Pt}/\text{Nb}_2\text{W}_{15}\text{O}_{50}$, which were assigned as belonging to the tetragonal phase WO_3 (PDF#85-0808). Considering that the ionic radius of Nb^{5+} (0.65 Å) is larger than that of W^{3+} (0.60 Å), this shifts the (110) spacing to a lower value when Nb^{5+} was incorporated into the WO_3 lattice. This change is linked to the formation of a solid solution structure, and such configuration has been described in detail by Li et al.²³ HAADF-STEM images further demonstrated that lattice distortion occurred in some regions, which was caused by the integration of Nb ions (Figure S4). Despite the observation that the tetragonal WO_3 phase was basically unchanged (as derived from the XRD results), the electrostatics in the crystal had become unbalanced in this process, resulting in a residual positive charge. Therefore, there is a tendency to adsorb anions induced by specific factors.²⁴ Moreover, the weak characteristic peak of Pt (red marked) in the XRD pattern demonstrates a smaller particle size and high dispersion of Pt nanoparticles, which is consistent with the conclusions of PSD and EDS.

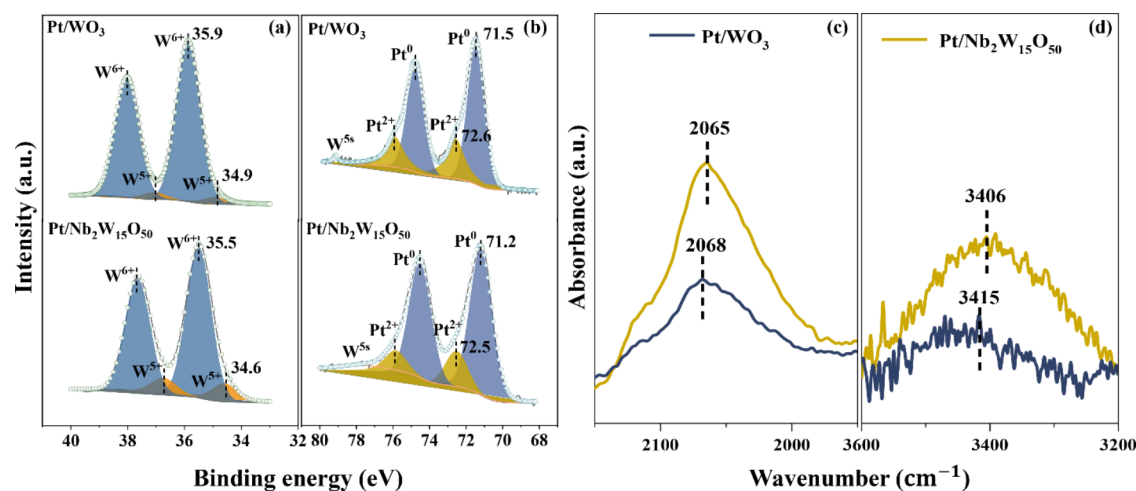


Figure 3. XPS spectra deconvolution result of Pt/Nb₂W₁₅O₅₀ and Pt/WO₃ catalysts, respectively. Pt 4f (a); W 4f (b). *In situ* DRIFTS of H₂ adsorption on Pt/WO₃ and Pt/Nb₂W₁₅O₅₀ (c, d).

Table 1. Catalytic Activity of Pt/Nb₂W₁₅O₅₀ and Other Catalysts^a

entry	catalysts	glycerol solution	conversion (%)	selectivity (%)				yield _{1,3-PDO} (%)
				1,3-PDO	1,2-PDO	<i>n</i> -PO	<i>i</i> -PO	
1	Pt/WO ₃	3 g, 20 wt %	25.9	49.9	5.6	37.5	7.4	12.9
2	Pt/Nb ₂ W ₁₅ O ₅₀	3 g, 10 wt %	78.7	62.0	3.5	28.2	6.3	48.9
3	Pt/Nb ₂ W ₁₅ O ₅₀	3 g, 20 wt %	72.6	66.5	2.4	23.7	7.5	48.2
4	Pt/Nb ₂ W ₁₅ O ₅₀	3 g, 30 wt %	68.2	65.3	3.3	22.3	9.1	44.6
5	Pt/Nb ₂ W ₁₅ O ₅₀	3 g, 40 wt %	64.2	65.2	2.2	25.4	7.3	41.9
6	Pt/Nb ₂ W ₁₅ O ₅₀	4 g, 20 wt %	69.8	65.5	1.8	28.1	4.6	45.7
7	Pt/Nb ₂ W ₁₅ O ₅₀	5 g, 20 wt %	66.0	65.6	1.8	28.0	4.7	43.3

^aOther reaction conditions: reaction time of 12 h, 1 MPa H₂ pressure, reaction temperature 130 °C, 0.2 g of catalyst, 3 wt % Pt loading.

Importance of Active Pt in Oxygen Vacancy Formation. Figure 2a displays the Raman spectra of Pt/WO₃ and Pt/Nb₂W₁₅O₅₀. The stretching vibration modes at 715 and 805 cm⁻¹ of Pt/WO₃ are assigned to the W–O–W oxygen bridge of WO₆ octahedra, while the two peaks at 271 and 324 cm⁻¹ were attributed to W–O vibrations.²⁵ Compared with Pt/WO₃, the integration of Nb broadened all vibration modes, while accompanied by a red shift. Such results mirror that abundant surface oxygen vacancies were formed on the Pt/Nb₂W₁₅O₅₀ catalyst.^{26,27}

H₂-TPR was used to further verify the oxide domain of the catalyst in a H₂ atmosphere (Figure 2b). The peak at 57–70 °C was ascribed to the reduction of Pt²⁺, while the peak near 353 °C was attributed to the reduction of WO_x species adjacent to Pt sites.²⁸ Interestingly, despite the identical Pt loading, a higher H₂ consumption was observed for Pt²⁺ on Pt/Nb₂W₁₅O₅₀ (0.164 cm³ g⁻¹) than for Pt/WO₃ (0.129 cm³ g⁻¹). Simultaneously, the significant shift of the reduction temperature (70 vs 57 °C) reflects that the integration of Nb induced an interaction with Pt. Moreover, compared with Pt/WO₃, the reduction peak within the range of 500–1000 °C over Pt/Nb₂W₁₅O₅₀ was increased by a factor of 5, and mirroring rich oxygen vacancies were generated *in situ*. In addition, H₂ consumption in the high-temperature regions of both supports was similar to Pt/WO₃, mirroring that individual support cannot form oxygen vacancies (Figure S5).

TGA was used to further investigate the origin of the oxygen vacancies (Figure 2c). No more than 2% mass loss occurred in Pt/WO₃ when the temperature rose to 800 °C in air, while Pt/Nb₂W₁₅O₅₀ had almost no mass loss, confirming the good

stability of both catalysts. Interestingly, the mass of Pt/Nb₂W₁₅O₅₀ even exerted a slight increase before 600 °C, this phenomenon may be caused by oxygen filling the vacancy or oxidation of Pt species.²⁹ However, the Pt/WO₃ catalyst and Nb₂W₁₅O₅₀ support do not conform to this trend. Combined with the H₂-TPR results, mirroring that Pt species on Pt/Nb₂W₁₅O₅₀ has a wider redox domain.

This could be easily observed by EPR measurements (Figures 2d and S6): a signal at a *g* value of 2.003 was attributed to the oxygen vacancies on Pt/Nb₂W₁₅O₅₀, while no signal of electron trapping was detected on the monoclinic phase Pt/WO₃. Filho et al. suggested that Nb₂O₅ was the cause of these defects.³⁰ To further clarify the origin of the oxygen vacancy, EPR analysis was performed for Nb₂W₁₅O₅₀ and WO₃, respectively. However, no oxygen vacancy was detected on both supports (Figure S6), demonstrating that the Nb₂W₁₅O₅₀ support cannot spontaneously induce electron transport and form oxygen vacancies *in situ* without the participation of Pt. Since these oxygen vacancies were only measured on the catalyst after H₂ reduction, given the electrostatic equilibrium, it is reasonable to assume that the electrons obtained on the oxygen vacancies were transferred from H₂ spillover.^{31,32} Combined with the TGA and H₂-TPR results, it can thus be hypothesized that the generation of these oxygen vacancies was triggered by active Pt on the support.

The surface chemical states of the catalyst after H₂ reduction were conducted by XPS (Figures 3a,b, S6–S7 and Table S2). The doublets with W 4f_{7/2} BEs of ca. 34.9 and 35.9 eV on Pt/WO₃ could be ascribed to W⁵⁺ and W⁶⁺, respectively.¹⁷ The doublets were shifted to lower binding energy of 34.6 and 35.5

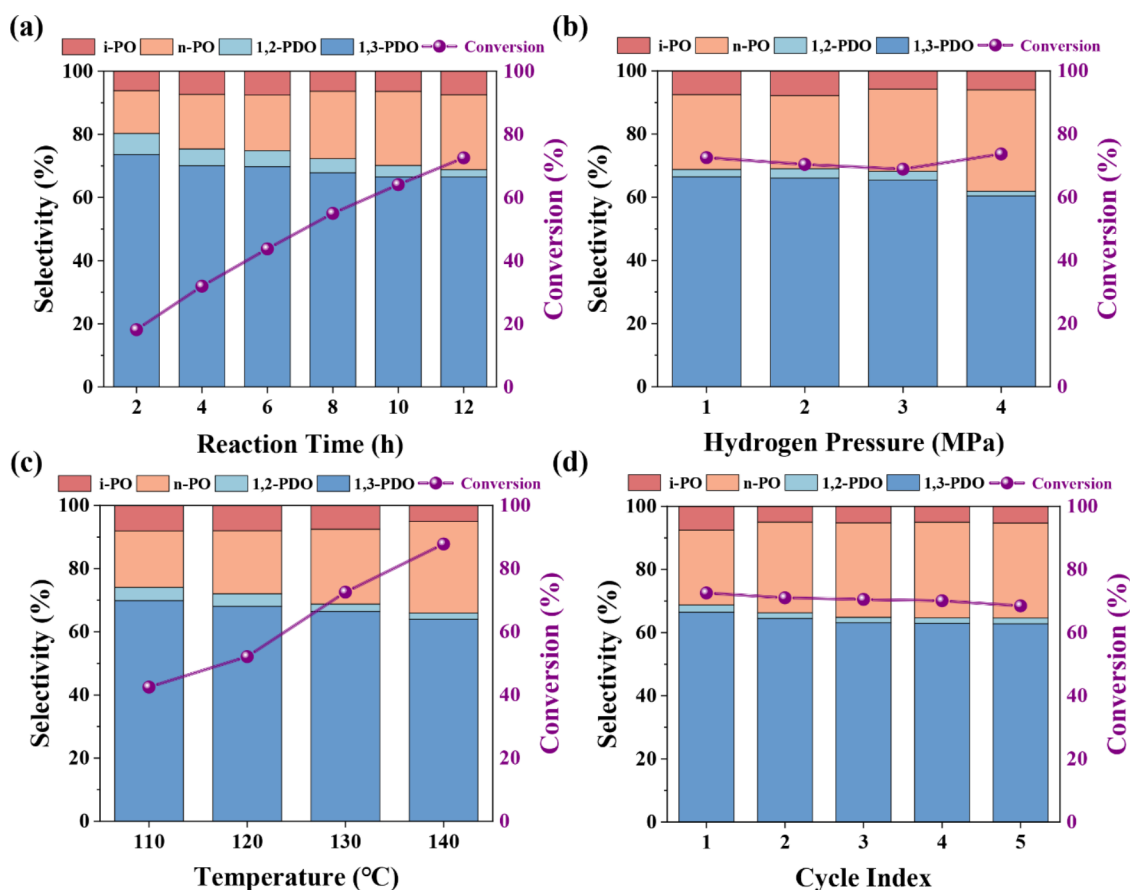


Figure 4. Catalytic performance of glycerol hydrogenolysis on Pt/Nb₂W₁₅O₅₀. (a) Product distributions of glycerol hydrogenolysis at different reaction times. (b) Effect of H₂ pressure on the catalytic performance. (c) Effect of reaction temperature on glycerol hydrogenolysis. (d) Stability test results of glycerol hydrogenolysis on Pt/Nb₂W₁₅O₅₀ (130 °C, 10 h). Note: reaction conditions: 130 °C, 1.0 MPa, 12 h, 3 wt % Pt loading, 0.2 g of catalyst, 3.0 g of 20 wt % glycerol solution.

eV on Pt/Nb₂W₁₅O₅₀, suggesting that some W species (presumably associated with oxygen vacancies) trapped electrons, causing the trapped electrons to be taken up by W nucleus.³³ This trend was also found in Pt 4f_{7/2} BEs of Pt/Nb₂W₁₅O₅₀, confirming a more conducive reduction of Pt species on Nb₂W₁₅O₅₀. However, XPS experiments were not strictly in situ tests, during which the catalyst was briefly exposed to air, which may trigger the oxidation of trace amounts of Pt. Compared with Pt/WO₃, the proportion of Pt and W in the low state was increased significantly, mirroring the presence of rich redox couples and frequent electron transport.³⁴ These results further identified the electron transfer between Pt and oxygen vacancies via H₂ spillover, which can accelerate the rate of redox reaction.³⁵ Moreover, the 4 Pt 4f_{7/2} BEs and W 4f_{7/2} BEs of Pt/Nb₂W₁₅O₅₀ did not change after the reaction. The proportions of Pt⁰ and W⁵⁺ showed small variations, which may be due to experimental errors in the testing process.

Catalyst Performance. The catalytic activity of catalysts was investigated for glycerol hydrogenolysis under conditions of 3 wt % Pt loading, 0.2 g of catalyst, 130 °C, 1.0 MPa H₂, 12 h, and 3 g of 20 wt % glycerol solution. As summarized in Table 1, Pt/WO₃ delivered a low glycerol conversion of 25.9% with 49.9% selectivity to 1,3-PDO (Entry 1). In contrast, Pt/Nb₂W₁₅O₅₀ gave a 75.6% conversion with 66.5% selectivity (Entry 3) under the same conditions, affording a 1,3-PDO yield of 48.2%, which was almost 4 times that of Pt/WO₃.

Noteworthy, Pt/Nb₂W₁₅O₅₀ was endowed with high selectivity to 1,3-PDO, and this selectivity is not reduced even at higher glycerol concentrations (Entries 4 and 5).

The product distribution of glycerol hydrogenolysis was investigated every 2 h on Pt/Nb₂W₁₅O₅₀ (Figure 4a). The glycerol conversion increased from 18.1 to 72.6% with an increase of reaction time from 2 to 12 h. The initial selectivity of the primary products 1,3-PDO and 1,2-propanediol (1,2-PDO) were 73.6 and 6.7% (2 h reaction time), respectively, implying a high selectivity for secondary C–O bond activation. In general, with the increase of reaction time, the excess hydrogenolysis of these diols will cause a continuously increasing yield of monohydric alcohols (*i*-propanol (*i*-PO) and *n*-propanol (*n*-PO)). However, the yield of *n*-PO increased significantly, while that of *i*-PO remained nearly constant. These results suggest that *n*-PO is the main product of 1,2-PDO hydrogenolysis. Moreover, isolated –OH groups were shown to be difficult to hydrolyze, and the presence of at least two adjacent –OH is a prerequisite for hydrogenolysis, which is consistent with the conclusion of Shishido et al.³⁶ In addition, when 1,3-PDO concentration was dominant, the reaction was dominated by the hydrogenolysis of the main product 1,3-PDO, leading to a rapid decrease in the selectivity to 1,3-PDO (Table S4).

In glycerol hydrogenolysis, H₂ dissociation and spillover are of significant importance to the dehydration and hydrogenation steps. In other words, it is a shortcut to optimize the

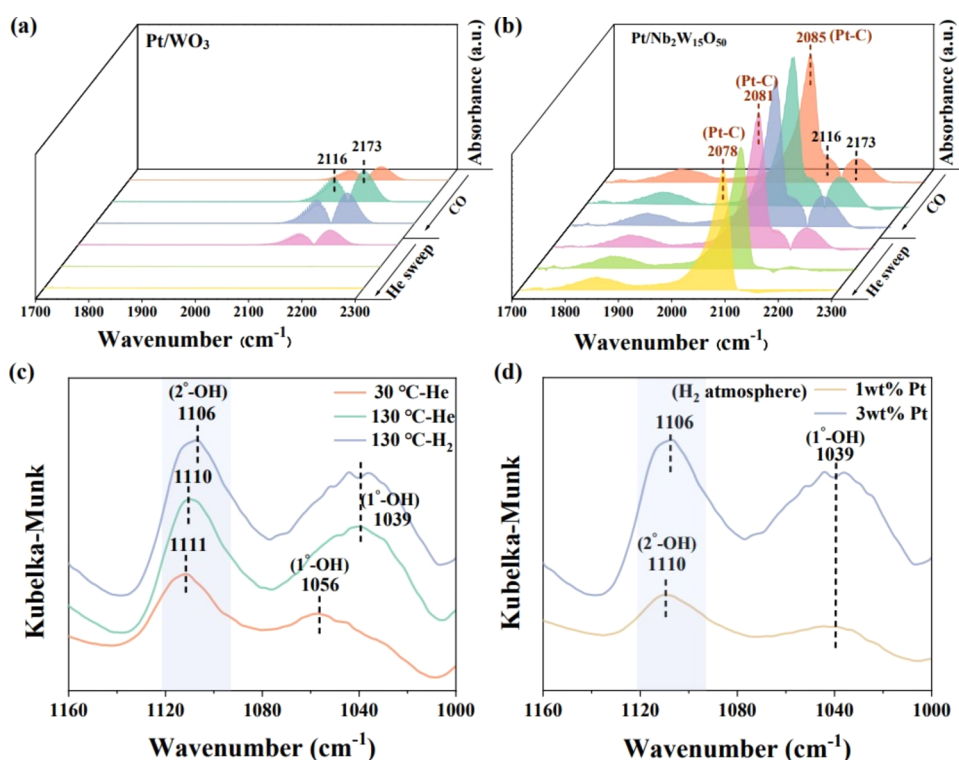


Figure 5. *In situ* DRIFTS of CO adsorption on Pt/WO₃ (a) and Pt/Nb₂W₁₅O₅₀ (b). *In situ* DRIFTS of glycerol hydrogenolysis on Pt/Nb₂W₁₅O₅₀ under different atmospheres and temperatures (c). *In situ* DRIFTS of glycerol hydrogenolysis on Pt/Nb₂W₁₅O₅₀ with different Pt loadings (d).

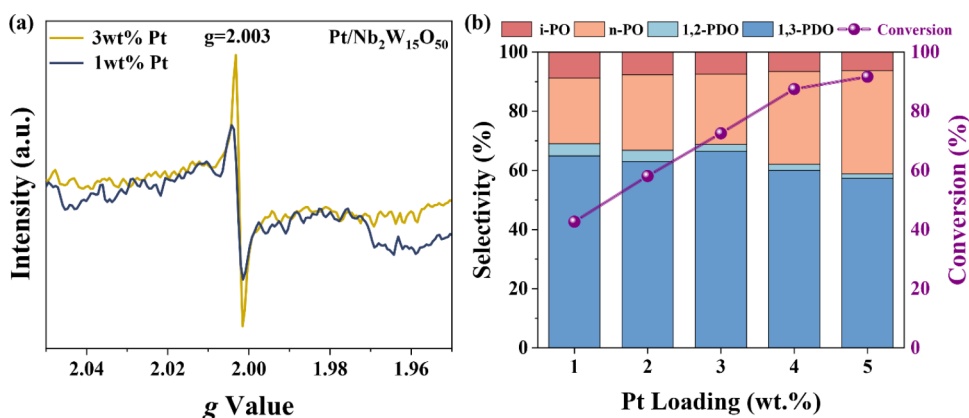


Figure 6. (a) EPR spectra of Pt/Nb₂W₁₅O₅₀ with different Pt loadings. (b) Effect of Pt load on glycerol hydrogenolysis on Pt/Nb₂W₁₅O₅₀ catalysts (130 °C, 12 h, 1 MPa, 0.2 g of catalyst, 3 g of 20 wt % glycerol solution).

catalytic performance if the catalyst can rationally utilize H₂ and maximize the H₂ dissociation ability. Encouragingly, Pt/Nb₂W₁₅O₅₀ exhibited a high hydrogenolysis activity also at low H₂ pressure (1 MPa), achieving a 1,3-PDO yield of still 48.2% (Figure 4b). As the H₂ pressure continuously increased, it was beneficial to the conversion of glycerol, but the selectivity of 1,3-PDO was not improved (Table S4). This mirrors that the H₂ activation ability can be saturated at lower pressure on Pt/Nb₂W₁₅O₅₀. In addition, the Nb-rich catalysts in the previous work are similar to most catalysts in that their catalytic activity shows a strong dependence on high H₂ pressure.¹⁰ Under the same conditions, only a 17.2% yield of 1,3-PDO was obtained on the Nb-rich catalyst (Table S4). This contrast further highlights the stronger H₂ activation capacity on Pt/Nb₂W₁₅O₅₀.

The influence of the reaction temperature on glycerol hydrogenolysis was investigated, and the results are displayed in Figure 4c. Increasing temperatures accelerated the reaction rate and drove the rapid hydrogenolysis of glycerol. A yield of 56.2% was obtained at 140 °C, which is the highest yield achieved so far under low-pressure conditions (1 MPa). The reusability of Pt/Nb₂W₁₅O₅₀ is examined in Figure 4d. After each reaction, the catalyst was recovered from the liquid phase and put into the next activity test without any treatment. Even though the yield of 1,3-PDO exhibited a slight decline after each reuse run, we attribute this decline in the catalytic performance to the loss of catalyst mass. However, only 5% of the yield was lost after five runs, indicating a passable reusability of Pt/Nb₂W₁₅O₅₀.

Structure–Performance Relationship. To establish the structure–performance relationship, *in situ* DRIFTS of CO

adsorption were obtained to investigate the effect of Pt and the support (Figure 5). Two peaks located at 2173 and 2116 cm^{-1} (Figure 5a) on Pt/WO₃ were assigned to CO adsorbed on the positively charged Pt and the linear adsorption of CO onto metallic Pt, respectively.³⁷ These two peaks result from the physical adsorption of CO, which is easy to remove under gentle He purging. In contrast, a strong chemisorption peak appeared at 2085 cm^{-1} on Pt/Nb₂W₁₅O₅₀ (Figure 5b), which is attributed to CO adsorbed on the active Pt.³⁸ This result proves that Nb₂W₁₅O₅₀ can provide a large amount of active Pt, which is essential for the overall redox reaction. The information on active Pt was further clarified by CO chemisorption (Table S5). The cumulative quantity of CO chemisorption on Pt/Nb₂W₁₅O₅₀ (1.502e-02) was much higher than that on Pt/WO₃ (5.506e-03), which was consistent with the results of CO-DRIFTS. In addition, the dispersion of active Pt on Pt/Nb₂W₁₅O₅₀ was much higher than that on Pt/WO₃, which may be one of the reasons affecting the catalytic performance. The *in situ* DRIFTS of H₂ adsorption further revealed the interaction between oxygen vacancies and active Pt. Figure 3d exhibits two peaks on the two catalysts, one peak at 3406–3415 cm^{-1} was ascribed to the stretching vibration of the O–H chelate,³⁹ while the other located at 2065–2068 cm^{-1} (Figure 3c) is interpreted as resulting from the vibration of hydride on the active Pt (Pt–H).²⁸ Importantly, the presence of Pt–H is a prerequisite for glycerol hydrogenolysis. The higher intensity of Pt–H peaks on Pt/Nb₂W₁₅O₅₀ compared with Pt/WO₃ confirms an increased ability of H₂ dissociation. This is the intrinsic impetus of Pt/Nb₂W₁₅O₅₀ for the exceptional hydrogenolysis activity at low H₂ pressure, which is the fundamental reason for the results in Figure 4b.

To prove the conclusion in reverse, the oxygen vacancy strength on Pt/Nb₂W₁₅O₅₀ with different Pt loadings was investigated by EPR (Figure 6a). The strength of oxygen vacancy on Pt/Nb₂W₁₅O₅₀ with 3 wt % Pt loading was significantly enhanced compared with 1 wt % Pt loading. Therefore, it can be considered that the amount of active Pt was positively correlated with the strength of oxygen vacancies. However, the relationship between these two active centers on the performance of the catalyst still needs to be further verified. For this purpose, the effect of different Pt loadings on catalytic performance was carried out (Figure 6b). The glycerol conversion showed a linear correlation with Pt loading, while 52.5% yield of 1,3-PDO was obtained at 5 wt % Pt loading. Nevertheless, a slight decrease in 1,3-PDO selectivity occurs when the Pt load exceeds 3 wt %, mirroring that 3 wt % Pt loading was capable of supplying the H₂ activation required for the hydrogenolysis. These *in situ* DRIFTS experiment with EPR and XPS results indicate a strong interaction between active Pt and oxygen vacancies through H₂ spillover. Under the premise that the utilization of active Pt is maximized (Pt loading ≤ 3 wt %), the yield of 1,3-PDO positively correlates with both active Pt and the strength of the oxygen vacancies.

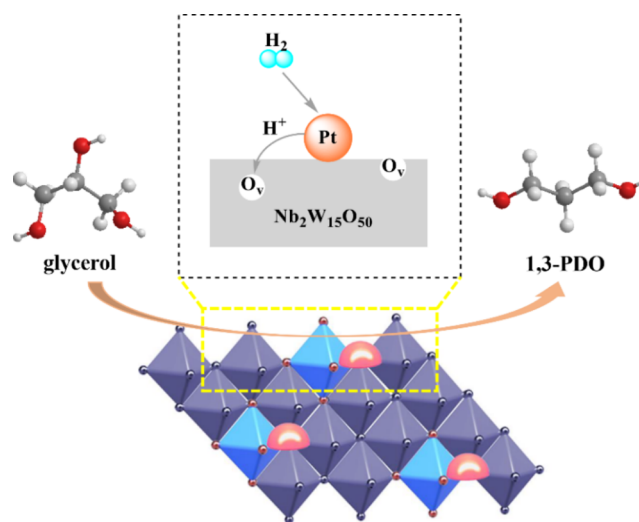
In situ DRIFTS data of glycerol hydrogenolysis were obtained to track the adsorption state on Pt/Nb₂W₁₅O₅₀. In a He atmosphere of 30 °C (Figure 5c), two absorption bands were observed at 1111 and 1056 cm^{-1} , corresponding to the stretching vibration of adsorbed 2° hydroxyl group (2°–OH) and 1° hydroxyl group (1°–OH), respectively.⁴⁰ When the temperature was increased to 130 °C, the adsorption strength of the two –OH groups on the catalyst was significantly enhanced. Particularly, the band of 1°–OH was shift from 1056 to 1039 cm^{-1} , indicating that 1°–OH was adsorbed by

the catalyst more easily than 2°–OH groups during the heating process. When the atmosphere was switched to H₂, an obvious red shift was observed on 2°–OH band (from 1110 to 1106 cm^{-1}), while the 1°–OH band was maintained at 1139 cm^{-1} . This phenomenon reveals that the secondary C–O bond interacted more strongly with the catalyst in the reaction.⁴¹ It can be considered that both –OH groups will be adsorbed by the catalyst in the reaction, while 2°–OH was activated as the main reaction.

Previously, Ma et al.¹² and Ren et al.⁴¹ through attenuated total reflectance-infrared (ATR-IR) spectroscopy combined with FTIR spectra of pyridine adsorption verified that the adsorption sites of 2°–OH and 1°–OH were corresponding to Brønsted acid and Lewis acid, respectively. According to their conclusions, Brønsted acid sites were generated *in situ* on Pt/Nb₂W₁₅O₅₀ during the reaction, which is the key to the high yield of 1,3-PDO. The NH₃-TPD results are shown in Figure S5. Compared with Pt/WO₃, the strong acid site of Pt/Nb₂W₁₅O₅₀ had almost disappeared, to be replaced by the dominant medium strong acid site. This suggests that a uniform and mildly acidic environment is more conducive to the formation of 1,3-PDO.

Subsequently, the reaction states of two types of –OH on Pt/Nb₂W₁₅O₅₀ with different Pt load were studied (Figure 5d). It was found that more Brønsted acid sites were generated with the increase of active Pt sites, which was manifested by the red shift and the increasing adsorption strength of 2°–OH bond. The generation of the Brønsted acid site is related to the strong interaction between active Pt and oxygen vacancies. Therefore, the structural property relationship of glycerol hydrolysis on Pt/Nb₂W₁₅O₅₀ can be illustrated as Scheme 1: The active Pt

Scheme 1. Catalytic mechanism of the active site on Pt/Nb₂W₁₅O₅₀



with strong H₂ dissociation ability has an interaction with the oxygen vacancies via H₂ spillover. In turn, oxygen vacancies can trap the hydrogen species from H₂ spillover, while rich Brønsted acid sites were generated *in situ*. However, due to the limitation of equipment conditions, the above characterization cannot strictly reproduce the actual working state of the catalyst. Therefore, the reaction mechanism of the catalyst in the actual working state is still restricted by many factors such as high temperature, H₂ pressure, agitation, and solvent, which needs to be further explored and improved.

CONCLUSIONS

A solid solution-supported catalyst Pt/Nb₂W₁₅O₅₀ with oxygen vacancies displayed a high catalytic performance under low H₂ pressure for glycerol hydrogenolysis to 1,3-PDO. The unique electronic environment of the Nb₂W₁₅O₅₀ solid solution stimulated a large number of active Pt sites, which significantly enhanced the H₂ dissociation ability. In turn, this active Pt is associated with the oxygen vacancies on the support via H₂ spillover and further induced the in situ formation of Brønsted acid sites and 1,3-PDO. The structure–performance relationship reveals that this synergistic effect can effectively connect the deoxygenation and hydrogenation steps in tandem, delivering a high glycerol conversion (75.6%) and 1,3-PDO selectivity (66.5%) under mild conditions (1 MPa, 130 °C). This study thus provides a new perspective for the in-depth study of the synergistic effects of metal–support dynamic interactions on catalytically active sites.

ASSOCIATED CONTENT

Supporting Information

The Supporting Information is available free of charge at <https://pubs.acs.org/doi/10.1021/acssuschemeng.3c08096>.

Nanoscale scale analysis of catalyst structure; N₂ sorption isotherm and the pore size distributions; XRD patterns of Pt/Nb₂W₁₅O₅₀ and Pt/WO₃; HAADF-STEM images of Nb₂W₁₅O₅₀; NH₃-TPD profiles of Pt/Nb₂W₁₅O₅₀ and Pt/WO₃; the specific surface area of samples; XPS analysis deconvolution result (PDF)

AUTHOR INFORMATION

Corresponding Authors

Qineng Xia – College of Biological, Chemical Science and Engineering, Jiaxing University, Jiaxing 314001, China; orcid.org/0009-0007-4143-3995; Email: xiaqineng@mail.zjxu.edu.cn

Shaomin Liu – College of Chemical Engineering, Beijing University of Chemical Technology, Beijing 100029, China; orcid.org/0000-0001-5019-5182; Email: liushaomin@buct.edu.cn

Authors

Jinghu Chen – College of Biological, Chemical Science and Engineering, Jiaxing University, Jiaxing 314001, China; College of Chemical Engineering, Beijing University of Chemical Technology, Beijing 100029, China

Hong Huang – College of Biological, Chemical Science and Engineering, Jiaxing University, Jiaxing 314001, China

Hu Pan – College of Biological, Chemical Science and Engineering, Jiaxing University, Jiaxing 314001, China

Yongyong Cao – College of Biological, Chemical Science and Engineering, Jiaxing University, Jiaxing 314001, China; orcid.org/0000-0002-4548-9087

Lingchang Jiang – College of Biological, Chemical Science and Engineering, Jiaxing University, Jiaxing 314001, China; orcid.org/0000-0003-2054-1851

Xiangtong Meng – College of Chemical Engineering, Beijing University of Chemical Technology, Beijing 100029, China; orcid.org/0000-0001-7250-4556

Jieshan Qiu – College of Chemical Engineering, Beijing University of Chemical Technology, Beijing 100029, China

Han Zuilhof – Laboratory of Organic Chemistry, Wageningen University, 6708WE Wageningen, The Netherlands; China-

Australia Institute for Advanced Materials and Manufacturing, Jiaxing University, Jiaxing 314001, China; orcid.org/0000-0001-5773-8506

Complete contact information is available at: <https://pubs.acs.org/10.1021/acssuschemeng.3c08096>

Author Contributions

J.C., H.H., H.P., and Y.C.: preparation and characterization of catalysts, and performing the catalytic reactions. J.C., L.J., and X.M.: collection and analysis of DRIFTS. J.C., Q.X., J.Q., H.Z., and S.L.: overall direction of the project. J.C., Q.X., and S.L.: wrote the manuscript with the help of all authors.

Notes

The authors declare no competing financial interest.

ACKNOWLEDGMENTS

This work was financially supported by the National Natural Science Foundation of China (No. 21972056), the Fundamental Research Fund for the Central University (Buctrc202115), and the Natural Science Foundation of Zhejiang Province (No. LY21B030008).

REFERENCES

- (1) Mizugaki, T.; Kaneda, K. Development of High Performance Heterogeneous Catalysts for Selective Cleavage of C-O and C-C Bonds of Biomass-Derived Oxygenates. *Chem. Rec.* **2019**, *19*, 1179–1198.
- (2) Yun, Y. S.; Berdugo-Díaz, C. E.; Flaherty, D. W. Advances in Understanding the Selective Hydrogenolysis of Biomass Derivatives. *ACS Catal.* **2021**, *11*, 11193–11232.
- (3) Lari, G. M.; Pastore, G.; Haus, M.; Ding, Y.; Papadokonstantakis, S.; Mondelli, C.; Pérez-Ramírez, J. Environmental and economical perspectives of a glycerol biorefinery. *Energy Environ. Sci.* **2018**, *11*, 1012–1029.
- (4) Pagliaro, M.; Ciriminna, R.; Kimura, H.; Rossi, M.; Della Pina, C. From Glycerol to Value-Added Products. *Angew. Chem., Int. Ed.* **2007**, *46*, 4434–4440.
- (5) Sun, D.; Yamada, Y.; Sato, S.; Ueda, W. Glycerol hydrogenolysis into useful C3 chemicals. *Appl. Catal., B* **2016**, *193*, 75–92.
- (6) Wang, J.; Yang, M.; Wang, A. Selective hydrogenolysis of glycerol to 1,3-propanediol over Pt-W based catalysts. *Chin. J. Catal.* **2020**, *41*, 1311–1319.
- (7) Bhowmik, S.; Darbha, S. Advances in solid catalysts for selective hydrogenolysis of glycerol to 1,3-propanediol. *Catal. Rev.* **2021**, *63*, 639–703.
- (8) Wu, F.; Jiang, H.; Zhu, X.; Lu, R.; Shi, L.; Lu, F. Effect of Tungsten Species on Selective Hydrogenolysis of Glycerol to 1,3-Propanediol. *ChemSusChem* **2021**, *14*, 569–581.
- (9) Che, T. M. Production of propanediols, US Patent 4642394, February 10, 1987. <https://patents.justia.com/patent/4642394>.
- (10) Chen, J.; Xia, Q.; Guo, Y.; Wang, Y.; Li, X.; Wang, M.; Qiu, J.; Wang, Y.; Sofianos, M. V.; Liu, S. Pt-Loaded Nb-W Metal Composite Oxide for Selective Cleavage of Secondary C-O Bonds. *Small* **2023**, *19*, No. 2304612.
- (11) Liu, L.; Asano, T.; Nakagawa, Y.; Gu, M.; Li, C.; Tamura, M.; Tomishige, K. Structure and performance relationship of silica-supported platinum-tungsten catalysts in selective C-O hydrogenolysis of glycerol and 1,4-anhydroerythritol. *Appl. Catal., B* **2021**, *292*, No. 120164.
- (12) Zhou, W.; Luo, J.; Wang, Y.; Liu, J.; Zhao, Y.; Wang, S.; Ma, X. WO_x domain size, acid properties and mechanistic aspects of glycerol hydrogenolysis over Pt/WO_x/ZrO₂. *Appl. Catal., B* **2019**, *242*, 410–421.
- (13) Lin, Z.; Liu, S.; Denny, S. R.; Porter, W. N.; Caratzoulas, S.; Boscoboinik, J. A.; Vlachos, D. G.; Chen, J. G. Experimental and Theoretical Insights into the Active Sites on WO_x/Pt(111) Surfaces

- for Dehydrogenation and Dehydration Reactions. *ACS Catal.* **2021**, *11*, 8023–8032.
- (14) Foo, G. S.; Wei, D.; Sholl, D. S.; Sievers, C. Role of Lewis and Brønsted Acid Sites in the Dehydration of Glycerol over Niobia. *ACS Catal.* **2014**, *4*, 3180–3192.
- (15) Musselwhite, N.; Na, K.; Sabyrov, K.; Alayoglu, S.; Somorjai, G. A. Mesoporous Aluminosilicate Catalysts for the Selective Isomerization of n-Hexane: The Roles of Surface Acidity and Platinum Metal. *J. Am. Chem. Soc.* **2015**, *137*, 10231–10237.
- (16) Fu, J.; Liu, S.; Zheng, W.; Huang, R.; Wang, C.; Lawal, A.; Alexopoulos, K.; Liu, S.; Wang, Y.; Yu, K.; Boscoboinik, J. A.; Liu, Y.; Liu, X.; Frenkel, A. I.; Abdelrahman, O. A.; Gorte, R. J.; Caratzoulas, S.; Vlachos, D. G. Modulating the dynamics of Brønsted acid sites on PtWO_x inverse catalyst. *Nat. Catal.* **2022**, *5*, 144–153.
- (17) Fan, Y.; Cheng, S.; Wang, H.; Tian, J.; Xie, S.; Pei, Y.; Qiao, M.; Zong, B. Pt-WO_x on monoclinic or tetrahedral ZrO₂: Crystal phase effect of zirconia on glycerol hydrogenolysis to 1,3-propanediol. *Appl. Catal., B* **2017**, *217*, 331–341.
- (18) Kyriakou, G.; Boucher, M. B.; Jewell, A. D.; Lewis, E. A.; Lawton, T. J.; Baber, A. E.; Tierney, H. L.; Flytzani-Stephanopoulos, M.; Sykes, E. C. H. Isolated Metal Atom Geometries as a Strategy for Selective Heterogeneous Hydrogenations. *Science* **2012**, *335*, 1209–1212.
- (19) Li, J.; Liu, H.-X.; Gou, W.; Zhang, M.; Xia, Z.; Zhang, S.; Chang, C.-R.; Ma, Y.; Qu, Y. Ethylene-glycol ligand environment facilitates highly efficient hydrogen evolution of Pt/CoP through proton concentration and hydrogen spillover. *Energy Environ. Sci.* **2019**, *12*, 2298–2304.
- (20) Im, J.; Shin, H.; Jang, H.; Kim, H.; Choi, M. Maximizing the catalytic function of hydrogen spillover in platinum-encapsulated aluminosilicates with controlled nanostructures. *Nat. Commun.* **2014**, *5*, No. 3370.
- (21) Zhou, W.; Zhao, Y.; Wang, Y.; Wang, S.; Ma, X. Glycerol Hydrogenolysis to 1,3-Propanediol on Tungsten/Zirconia-Supported Platinum: Hydrogen Spillover Facilitated by Pt(1 1 1) Formation. *ChemCatChem* **2016**, *8*, 3663–3671.
- (22) Yan, D.; Li, Y.; Huo, J.; Chen, R.; Dai, L.; Wang, S. Defect Chemistry of Nonprecious-Metal Electrocatalysts for Oxygen Reactions. *Adv. Mater.* **2017**, *29*, No. 1606459.
- (23) Wang, J.; Li, G.; Li, Z.; Tang, C.; Feng, Z.; An, H.; Liu, H.; Liu, T.; Li, C. A highly selective and stable ZnO-ZrO₂ solid solution catalyst for CO₂ hydrogenation to methanol. *Sci. Adv.* **2017**, *3* (10), No. e1701290, DOI: 10.1126/sciadv.1701290.
- (24) Zhu, K.; Shi, F.; Zhu, X.; Yang, W. The roles of oxygen vacancies in electrocatalytic oxygen evolution reaction. *Nano Energy* **2020**, *73*, No. 104761.
- (25) Wolcott, A.; Kuykendall, T. R.; Chen, W.; Chen, S.; Zhang, J. Z. Synthesis and Characterization of Ultrathin WO₃ Nanodisks Utilizing Long-Chain Poly (ethylene glycol). *J. Phys. Chem. B* **2006**, *110*, 25288–25296.
- (26) Solvothermal fabrication of Bi₂MoO₆ nanocrystals with tunable oxygen vacancies and excellent photocatalytic oxidation performance in quinoline production and antibiotics degradation. *Chin. J. Catal.* **2022**, *432*–472–484. DOI: 10.1016/S1872-2067(21)63876-7.
- (27) Yan, J.; Wang, T.; Wu, G.; Dai, W.; Guan, N.; Li, L.; Gong, J. Tungsten Oxide Single Crystal Nanosheets for Enhanced Multi-channel Solar Light Harvesting. *Adv. Mater.* **2015**, *27*, 1580–1586.
- (28) Miao, G.; Shi, L.; Zhou, Z.; Zhu, L.; Zhang, Y.; Zhao, X.; Luo, H.; Li, S.; Kong, L.; Sun, Y. Catalyst Design for Selective Hydrodeoxygenation of Glycerol to 1,3-Propanediol. *ACS Catal.* **2020**, *10*, 15217–15226.
- (29) Huang, Y.; Li, K.; Li, S.; Lin, Y.; Liu, H.; Tong, Y. Ultrathin Bi₂MoO₆ Nanosheets for Photocatalysis: Performance Enhancement by Atomic Interfacial Engineering. *ChemistrySelect* **2018**, *3*, 7423–7428.
- (30) Filho, D. d. A. B.; Franco, D. W.; Filho, P. P. A.; Alves, O. L. Niobia films: surface morphology, surface analysis, photoelectrochemical properties and crystallization process. *J. Mater. Sci.* **1998**, *33*, 2607–2616.
- (31) Wang, J.; Zhao, X.; Lei, N.; Li, L.; Zhang, L.; Xu, S.; Miao, S.; Pan, X.; Wang, A.; Zhang, T. Hydrogenolysis of Glycerol to 1,3-propanediol under Low Hydrogen Pressure over WO_x-Supported Single/Pseudo-Single Atom Pt Catalyst. *ChemSusChem* **2016**, *9*, 784–790.
- (32) Wan, J.; Chen, W.; Jia, C.; Zheng, L.; Dong, J.; Zheng, X.; Wang, Y.; Yan, W.; Chen, C.; Peng, Q.; Wang, D.; Li, Y. Defect Effects on TiO₂ Nanosheets: Stabilizing Single Atomic Site Au and Promoting Catalytic Properties. *Adv. Mater.* **2018**, *30*, No. 1705369.
- (33) Wei, Z.-W.; Wang, H.-J.; Zhang, C.; Xu, K.; Lu, X.-L.; Lu, T.-B. Reversed Charge Transfer and Enhanced Hydrogen Spillover in Platinum Nanoclusters Anchored on Titanium Oxide with Rich Oxygen Vacancies Boost Hydrogen Evolution Reaction. *Angew. Chem., Int. Ed.* **2021**, *60*, 16622–16627.
- (34) Yang, Y.; Zhu, H.; Xiao, J.; Geng, H.; Zhang, Y.; Zhao, J.; Li, G.; Wang, X.-L.; Li, C. C.; Liu, Q. Achieving Ultrahigh-Rate and High-Safety Li⁺ Storage Based on Interconnected Tunnel Structure in Micro-Size Niobium Tungsten Oxides. *Adv. Mater.* **2020**, *32*, No. 1905295.
- (35) Yu, K.; Lou, L.-L.; Liu, S.; Zhou, W. Asymmetric Oxygen Vacancies: The Intrinsic Redox Active Sites in Metal Oxide Catalysts. *Adv. Sci.* **2020**, *7*, No. 1901970.
- (36) Aihara, T.; Miura, H.; Shishido, T. Investigation of the mechanism of the selective hydrogenolysis of CO bonds over a Pt/WO₃/Al₂O₃ catalyst. *Catal. Today* **2020**, *352*, 73–79.
- (37) Zhang, Z.; Zhu, Y.; Asakura, H.; Zhang, B.; Zhang, J.; Zhou, M.; Han, Y.; Tanaka, T.; Wang, A.; Zhang, T.; Yan, N. Thermally stable single atom Pt/m-Al₂O₃ for selective hydrogenation and CO oxidation. *Nat. Commun.* **2017**, *8*, No. 16100.
- (38) DeRita, L.; Dai, S.; Lopez-Zepeda, K.; Pham, N.; Graham, G. W.; Pan, X.; Christopher, P. Catalyst Architecture for Stable Single Atom Dispersion Enables Site-Specific Spectroscopic and Reactivity Measurements of CO Adsorbed to Pt Atoms, Oxidized Pt Clusters, and Metallic Pt Clusters on TiO₂. *J. Am. Chem. Soc.* **2017**, *139*, 14150–14165.
- (39) Zhou, H.; Chen, L.; Guo, Y.; Liu, X.; Wu, X.-P.; Gong, X.-Q.; Wang, Y. Hydrogenolysis Cleavage of the Csp₂–Csp₃ Bond over a Metal-Free NbOPO₄ Catalyst. *ACS Catal.* **2022**, *12*, 4806–4812.
- (40) García-Fernández, S.; Gandarias, I.; Requies, J.; Soulimani, F.; Arias, P. L.; Weckhuysen, B. M. The role of tungsten oxide in the selective hydrogenolysis of glycerol to 1,3-propanediol over Pt/WO_x/Al₂O₃. *Appl. Catal., B* **2017**, *204*, 260–272.
- (41) Yang, M.; Wu, K.; Sun, S.; Ren, Y. Regulating oxygen defects via atomically dispersed alumina on Pt/WO_x catalyst for enhanced hydrogenolysis of glycerol to 1,3-propanediol. *Appl. Catal., B* **2022**, *307*, No. 121207.